https://doi.org/10.5194/tc-2022-152
Preprint. Discussion started: 31 August 2022

The Cryosphere Discussions

Modelled 3D calving at Kronebreen, Svalbard, driven by tidal fluctuations and frontal melt

Felicity A. Holmes[1], Eef van Dongen[2], Riko Noormets[3], Michał Pętlicki[4], and Nina Kirchner[1]

[1]Department of Physical Geography, Stockholm University, Sweden
[2]Department of Meteorology, Stockholm University, Sweden
[3]Department of Arctic Geology, University Centre in Svalbard, Longyearbyen, Svalbard, Norway
[4]Faculty of Geography and Geology, Jagiellonian University in Kraków, Cracow, Poland

Correspondence: Felicity A. Holmes (felicity.holmes@natgeo.su.se)

Abstract. Understanding calving processes and their controls is of importance for reducing uncertainty in sea level rise estimates. The impact of tidal fluctuations and frontal melt on calving patterns has been researched through both modelling and observational studies, but remain uncertain and may vary from glacier to glacier. In this study, we isolate various different impacts of tidal fluctuations on a glacier terminus to understand their influence on calving dynamics at Kronebreen, Svalbard, for the duration of one month. In addition, we impose frontal melt onto the calving front in order to allow for an undercut to develop over the course of the simulations. We find that calving events show a tidal signal when there is a small or no undercut but, after a critical point, undercut driven calving becomes dominant and drowns out the tidal signal. However, the relationship is complex and large calving events show a tidal signal even with a large modelled undercut. The modelled undercut sizes are then compared to observational profiles, showing that undercuts of up to c. 25 m are plausible. These findings highlight the complex interactions occurring at the calving front of Kronebreen and suggest further observational data and modelling work is needed to fully understand the hierarchy of controls on calving.

1 Introduction

Worldwide, glaciers have been losing mass during recent decades, with these mass losses contributing to eustatic sea level rise. Different elements of the cryosphere are contributing varying amounts; between 2006 and 2015, Greenland contributed 0.77 mm yr^{-1}, glaciers non-periphal to Greenland and Antarctica 0.61 mm yr^{-1}, and Antarctica 0.43 mm yr^{-1} (IPCC, 2019). One of the biggest hurdles to effective management of and adaptation to rising sea levels is having good projections of the future. To produce those, increased understanding of certain glaciological processes is required, especially along the marine ice margins. Mass loss originating from these areas is of significance; it is estimated that between 32 and 67 % of mass loss from Greenland is due to calving (Rignot and Kanagaratnam, 2006; Enderlin et al., 2014). When considering both calving and submarine melt (together: frontal ablation), around one third of Greenland's net mass loss between 2000 and 2012 can be attributed to their combined effect (King et al., 2020). Since 2013, this contribution has been over 50% as a result of a less negative surface mass balance (King et al., 2020). For Svalbard, estimates have put the contribution of calving in the range of 17 - 25 % of total mass loss (Błaszczyk et al., 2009). No more recent studies have been conducted to give updated estimates of calving fluxes for

https://doi.org/10.5194/tc-2022-152
Preprint. Discussion started: 31 August 2022

the whole of Svalbard (Schuler et al., 2020). However, studies on individual glaciers have shown considerable variability in calving losses with, for example, the 2012-2013 Austfonna surge potentially causing a doubling in the frontal ablation losses from Svalbard for this period and highlighting the need for updated estimates of frontal ablation (Dunse et al., 2012; Schuler et al., 2020). In addition, there is evidence that submarine melting may be of considerable importance for the frontal ablation of Svalbard glaciers (e.g. Luckman et al. 2015). At Antarctica, both melting from the ocean and calving/ice-shelf collapse have had large impacts on overall mass loss in recent decades (Shepherd et al., 2018). Between 1992 and 2017, submarine melt led to an increased mass loss in West Antarctica of 106 ± 55 billion tonnes of ice per year (Shepherd et al., 2018). During the same time period, ice-shelf collapse led to an increased mass loss of 26 ± 29 billion tonnes per year from the Antarctic Peninsula (Shepherd et al., 2018). Improved understanding of calving events and their triggers is crucial as iceberg calving and frontal melt have been shown to impact glacier dynamics far upstream of the margin, through a positive feedback loop which causes acceleration, thinning, and further retreat - as has been described for Jakobshavn Isbrae after the breakup of its ice tongue (Holland et al., 2008; Price et al., 2011; Christoffersen et al., 2011).

Mass losses at the ice - ocean interface from calving and submarine melt have been linked to increasing ocean temperatures (Christoffersen et al., 2011; Luckman et al., 2015; Holmes et al., 2019). However, atmospheric temperatures are also of importance through their ability to increase surface melt levels. This surface melt can then make its way into the subglacial hydrological system, where it is combined with water produced by basal melting (Karlsson et al., 2021). These waters subsequently exit the glacier at its terminus as a buoyant plume which rises through the water column whilst turbulently entraining warm waters residing at depth, if present, and exacerbating melt (Jenkins, 2011; Slater et al., 2017).

Alongside ocean and atmospheric temperatures, various other variables can act to trigger or modulate frontal ablation. For example, fjord topography and bathymetry can stabilise glacier fronts or block the intrusion of warm waters which might otherwise reach the grounding line where they could cause enhanced submarine melt (Jakobsson et al., 2020; Holmes et al., 2021). Sea level fluctuations, most notably due to tidal phase (falling vs rising tide), and ice mélange buttressing are examples of other factors which have received interest with regards to their importance for modulating the occurrence of calving (e.g. Todd and Christoffersen (2014); Bartholomaus et al. (2015); How et al. (2019)).

Here, we aim to provide some insight into how changing sea levels and frontal melt may influence calving patterns at Kronebreen, Svalbard via the use of numerical modelling. We start from a simulation where the combined effects of tidal variations, frontal melt, and calving are all included. We use tidal input data from August 2016 due to the availability of observations of both the sub-aerial and submarine portions of calving front morphology from the 16 Aug 2016, providing a rare opportunity to compare modelled and observed calving front geometry. However, due to simplifications in the model set-up that allow us to isolate tidal impact, the results are best viewed as a conceptual study that allows comparison of undercut magnitude rather than a direct representation of conditions during this time period. The various impacts of tidal fluctuations on calving are then investigated with the effects of changing back pressure, changing water levels in crevasses, and changing frontal melt locations all being tested separately.

https://doi.org/10.5194/tc-2022-152
Preprint. Discussion started: 31 August 2022

2 Study Area

Kronebreen, located on the west coast of Spitsbergen at 78.8N, 12.6E, is a fast flowing, grounded glacier (see Fig.1). Near its c. 3.6 km wide terminus (Holmes et al., 2019), Kronebreen shares a lateral margin with the much slower neighbouring glacier Kongsvegen, with both glaciers then terminating in Kongsfjorden. Kronebreen is fed by Holtedahlfonna and Infantfonna, with a total combined area of 372 km^2 (Schellenberger et al., 2015). In Kronebreen's lower reaches, it is heavily crevassed with flow speeds that can reach up to 5 m d^{-1} during summer (Schellenberger et al., 2015). Velocities, however, vary both seasonally and interannually, with these fluctuations attributed to the seasonal development of the basal hydrological system and variations in supra-glacial melt (Schellenberger et al., 2015; Vallot et al., 2017). Kronebreen has experienced increasing levels of melt in recent decades, with supraglacial melt during 2000-2012 having increased by 21% when compared to data from 1961-1999 - likely as a consequence of increased atmospheric temperatures (Van Pelt et al., 2012). Kongsfjorden has a length of 22 km and a width of between 4 and 12 km, making it wide enough for the Coriolis force to impact on circulation (Svendsen et al., 2002; Trusel et al., 2010). Kongsfjorden does not have a defined sill but does exhibit variable bathymetry that ranges from c. 400 m to c. 60 m. The fact that there is no defined sill means that intrusions of warm, Atlantic water (> 3°C) are able to enter Kongsfjorden and, potentially, reach the calving front of Kronebreen (Svendsen et al., 2002). Kongsfjorden's location on Svalbard's Western coast means that it is in close proximity to the West Spitsbergen current and so is subject to a wide range of different water masses (Nilsen et al., 2008). Previous work in the area has confirmed the presence of Atlantic waters in the fjord, with potential impacts for Kronebreen and neighbouring glacier Kongsvegen (Cokelet et al., 2008; Promińska et al., 2017). The water masses present in the fjord vary both seasonally and between years as the proportions of Arctic waters, Atlantic waters, and glacially-derived waters do not remain constant. Due to this variability, Kongsfjorden can either be in a 'cold mode' or a 'warm mode' depending on the amount of Atlantic water present (Cottier et al., 2005). From investigation of optical satellite imagery, two distinct subglacial plumes can be identified at the terminus of Kronebreen; one in the North and one in the South (see Fig. 1). Previous studies have found that the frontal ablation rate of Kronebreen is strongly correlated with fjord water temperatures, suggesting that fjord circulation and the aforementioned subglacial plumes are likely important drivers of mass loss at the terminus (Luckman et al., 2015; Holmes et al., 2019). In addition, a mass budget for Kronebreen between 2009 and 2014 found that frontal ablation accounted for around 84 % of total mass loss (Deschamps-Berger et al., 2019).

3 Methods

3.1 Modelling domain and set-up

This modelling study was carried out using Elmer/Ice (version 9.0), a finite element, full-Stokes, three-dimensional ice-sheet and glacier-flow model (Gagliardini et al., 2013), with a calving implementation based on the calving depth criterion (Benn et al., 2007; Todd et al., 2018). The code for Elmer/Ice is open source and freely available at github.com/ElmerCSC/elmerfem.

https://doi.org/10.5194/tc-2022-152
Preprint. Discussion started: 31 August 2022

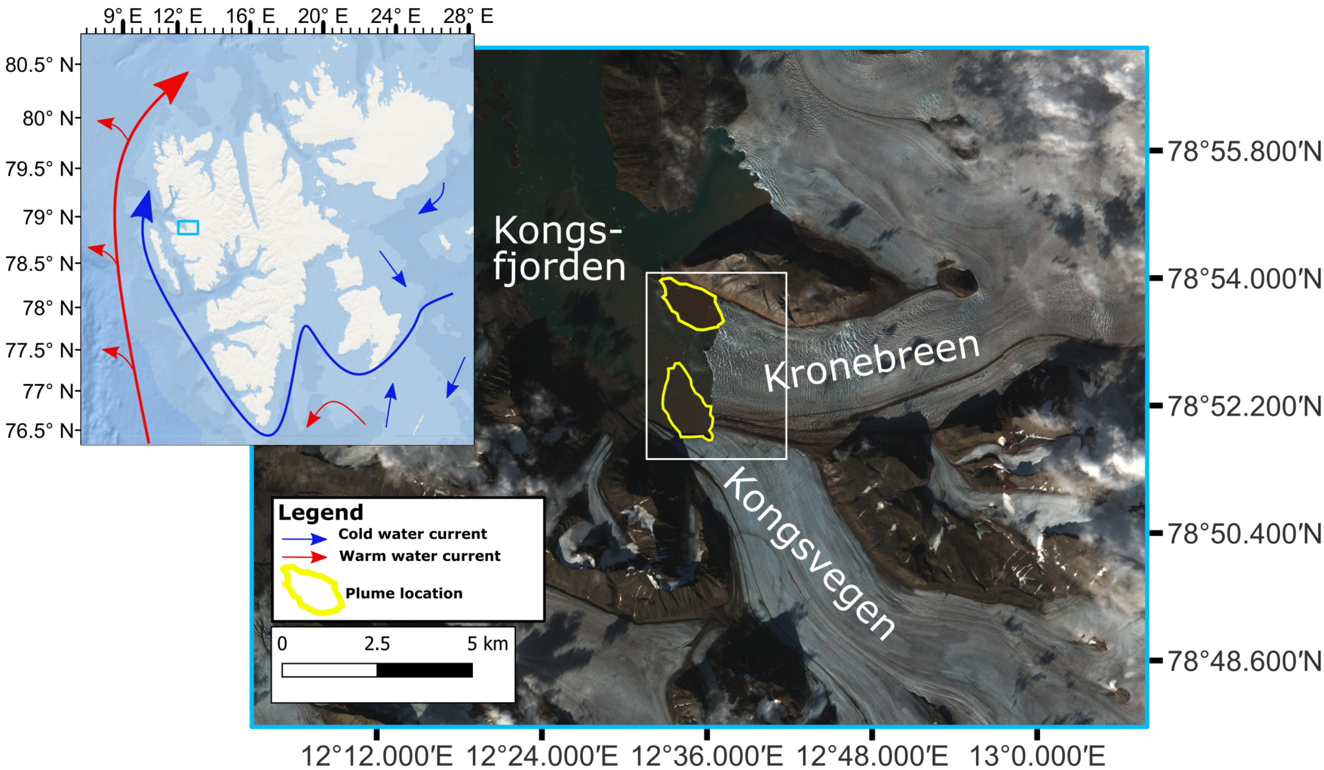

Figure 1. Location of Kronebreen on Svalbard (inset) and close-up showing the heavily crevassed frontal section of Kronebreen, as well as Kongsfjorden and Kongsvegen from August 2016 (right). The location of ocean currents present around Svalbard, adapted from Sundfjord et al. (2017), are shown on the inset figure: West Spitsbergen Current (warm waters) - red; cold currents - blue. Main image: The yellow polygons denote the location on subglacial plumes. The white box delineates the area shown in Fig. 4(a). Main image from source: Copernicus Sentinel data 2022. Retrieved from Copernicus Open Access Hub 23/05/2022, processed by ESA. Inset background image from Source: Esri, DigitalGlobe, GeoEye, Earthstar Geographics, CNES/Airbus DS, USDA, USGS, AeroGRID, IGN, and the GIS User Community.

The model domain (Fig. 2) is based on that used by Vallot et al. (2018) but altered to give the calving front its satellite-derived summer 2016 position. This was done to provide some consistency between the model domain and the tidal forcing, which is derived from observations taken in August 2016. However, the model set-up is designed to be diagnostic of how tides impact calving rather than to represent a certain time period as accurately as possible. Mesh resolution varied from 100 m at the front to 2000 m at locations furthest from the calving front (Fig. 2). A separate 2D planar mesh is created over the frontal area in order to determine crevasse propagation (Todd et al., 2018) and, for this planar mesh, a higher resolution of 10 m was used to allow for small calving events to be identified. The main 3D mesh was internally extruded to have 10 vertical layers, rendering a resolution of c. 10 m at the front. Five different types of mesh boundaries were implemented; an ice-ocean boundary (at the calving front), an ice-ice boundary (e.g. the confluence of Kongsvegen and Kronebreen), an ice-rock boundary (at the fjord walls), and the basal and the upper surface of the glacier, derived from data by Lindbäck et al. (2018). A linear type Weertman

https://doi.org/10.5194/tc-2022-152
Preprint. Discussion started: 31 August 2022

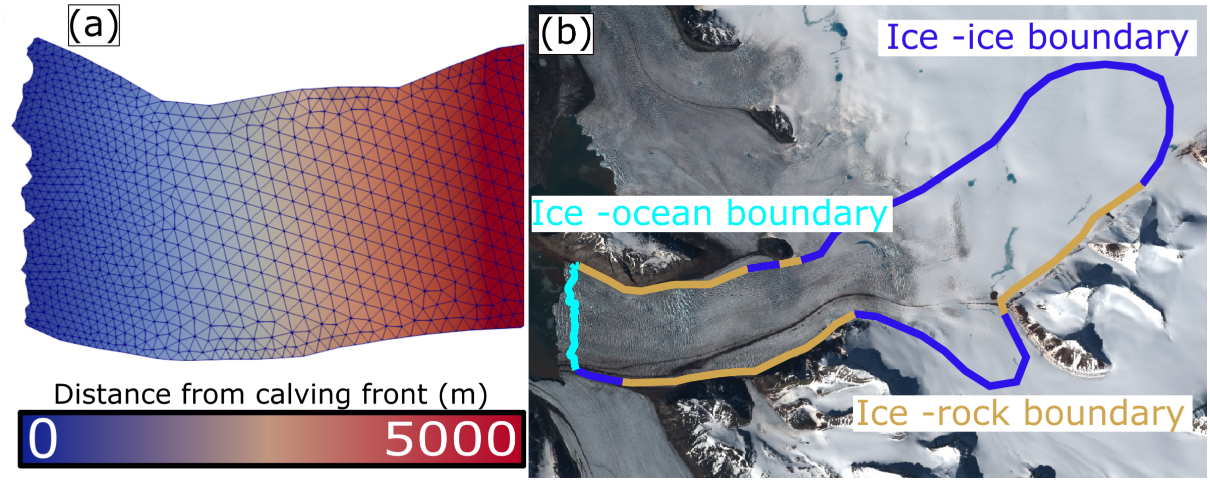

Figure 2. (a): View of frontal part of the mesh from above, with the different element sizes shown, which are smallest at the calving front and get larger with distance from the calving front. (b): The mesh domain and boundaries are shown, overlain on a Sentinel - 2 satellite image. The glacier margin is c. 3.3 km wide and the distance along a central flowline is c. 28 km. Background image for panel (b): Copernicus Sentinel data 2016, retrieved from Copernicus Open Access Hub 2022, processed by ESA.

(1974) friction law is applied at the base, and stress-free conditions are prescribed at the surface. For each tidal simulation, the entire month of August 2016 was simulated at 10 minute intervals. Different time step sizes and simulation lengths were used for the spin up and relaxation simulations (see Sec. 3.3).

3.2 Model inputs

For model initiation, and model forcing during the simulations, four variables are of particular relevance: satellite-derived surface glacier velocities (for basal friction inversions and inflow velocities at the ice-ice boundaries), surface temperatures (for use in the thermodynamic spin-up), sea level (tidal) fluctuations (for use as a forcing in the main suite of simulations), and submarine frontal melt (FM, to account for the impact of oceanic heat on processes at the calving front).

The variables are harvested from the following sources: Ice surface velocities are calculated from Sentintel-1 GRDH SAR images (Copernicus Sentinel data (2016)) via offset tracking (e.g. Strozzi et al., 2002) of orbitally corrected and co-registered image pairs with a grid azimuth and range spacing of 10 pixels, corresponding to a resolution of 100 m. A summer (3rd - 15th July 2016) and a winter (30th November to 6th December 2016) velocity field were calculated.

Surface air temperature (2m), as well as surface mass balance (SMB) and its component parts (snowfall, rain, runoff, refreezing and retention, and melt), are provided in a data set by Noël et al. (2020) at a 500 m spatial and daily temporal resolution.

Tidal fluctuations from measurements taken every 10 minutes at Ny Ålesund, Svalbard (c. 17 km from Kronebreen's terminus), were collected from kartverket.no and define the temporal changes of sea level in the model. The data from kartverket.no are provided with reference to the mean water level observed during the period 1996–2014. These data determine the propor-

https://doi.org/10.5194/tc-2022-152
Preprint. Discussion started: 31 August 2022

tions of the calving front that are submerged below or exposed above the waterline, and hence where sea pressure ('SP') is exerted, where frontal melt ('FM') occurs, and which minimal crevasse depth ('CD') is required for a surface crevasse to reach sea level and lead to calving due to hydrofracture, cf. Sect. 3.3 and Benn et al. (2007). As the tidal fluctuations cover a month long period, the tidal amplitude varies over the course of the simulations with both spring and neap tides being present.

For simulations where FM was applied, both its location and magnitude was kept constant during the simulations. The background level of melt was set at 500 m yr^{-1}, and the high melt (plume) level was set at 1500 m yr^{-1}. Previous estimates of FM at Kronebreen have suggested winter lows ranging from c. 30 to c. 400 m yr^{-1} and summer highs ranging from c. 300 to c. 2300 m yr^{-1} (Holmes et al., 2019; Köhler et al., 2019). As a summer scenario is in focus here, the background and plume melt values were chosen so that they fit within the summer FM estimate range. However, the FM parameterisation used here is simple and further study is needed to better constrain frontal melt rates at Kronebreen. The location of the high melt (plume) areas along the calving front (Fig. 1) were informed by the visual inspection of optical Landsat 8 satellite images from 2016 and 2017. FM is, by definition, only applied below the waterline, with values of 0 m yr^{-1} prescribed for sub-aerial parts of the terminus. These FM values allowed for an undercut to develop during the course of the simulations, providing insight into how frontal morphology may impact calving.

3.3 Simulation workflow

The workflow consisted of five stages: I. inversions for basal friction, II. a fixed-geometry 500 year thermodynamic spin-up, III. a 125 day relaxation simulation with calving and front movement permitted, IV. the main simulations, a suite of seven runs, with a freely evolving ice surface and fully active calving front, V. post-processing, during which the percentage of calving events in each simulation occurring on a rising tide and a falling tide was investigated, both for calved icebergs of any size, and for large (> 500 m^3) icebergs. In addition, the absolute water depth at which calving events occurred was investigated and calving frequency was related to tidal amplitude.

In numerical ice flow simulations, basal friction has to either be prescribed, or be computed from observed ice surface velocities using inverse approaches (e.g. Gillet-Chaulet et al. (2012); Vallot et al. (2017)). Here, we follow Arthern and Gudmundsson (2010) who employed the Robin inverse method to invert surface velocities for basal friction, now distributed as part of Elmer/Ice (cf. Sect. A1 and Fig. A1). Separate inversions were done for winter and summer using velocity fields derived from offset tracking (see Sect. 3.2), as levels of basal and surface melt vary seasonally and can lead to large variations in basal friction at Kronebreen (Vallot et al., 2017). Basal friction, a parameter in the sliding law, was subsequently modelled as a sinusoidally varying curve with the two inverted fields as maximum and minimum values during stages II and III. The maximum field was from winter (30 Nov 2016 to 06 Dec 2016) and the minimum field from summer (03 July 2016 to 15 July 2016, see Fig. A2).

A fixed geometry spin-up simulation with temperature forcing corresponding to average temperatures for the years 2000-2018 was then run. The only output variables that were allowed to develop with time were velocity and temperature (e.g. Sato and Greve (2012); Seddik et al. (2012)). The spin-up was run for 500 years at monthly time steps until reaching a steady state, which was identified from the lack of a directional trend in the time series of temperatures and velocities (cf. Sect. A1).

As fixed geometry spin-ups can lead to artificial drift after surfaces are allowed to evolve (Le Clec'h et al., 2019), a relaxation simulation was run for 500 time steps of 0.25 days each after the spin-up (cf. Sect. A1 and Fig. A2). In this step, and for all further steps, the temperature field was set to be constant and equalled the results of step II. For the relaxation simulation, there was still no SMB forcing, but calving and frontal melt (at a constant 500 m yr^{-1}) were activated to allow for relaxation of the terminus geometry. These simulations used the Calving3D solver, which is based on the calving depth criterion (Benn et al., 2007), implemented into Elmer/Ice and evaluated for Store Glacier, Central West Greenland by Todd et al. (2018). This solver facilitates calving via one of two mechanisms; either surface crevasses and basal crevasses meet and imply fracture from the surface to the base (mechanism 'base'), or surface crevasses extend to the waterline where crevasse propagation to the ice base takes place through hydrofracture (mechanism 'surf'). To accommodate for changes in calving front geometry induced by calving events, the 3D mesh is updated after each calving event. In this stage, only limited calving was permitted by limiting the area over which calving could occur to points within 50 m of the terminus.

The modelled configuration of Kronebreen at the end of stage III served as starting point for the seven main simulations in stage IV (see Fig. A2). These have in common that they were each run for 31 days, at a time step of 10 minutes wall clock time. Basal friction was set to equal the result of the summer inversion and was kept constant throughout all the simulations. No SMB forcing was included and frontal melt (now including plumes) was kept temporally constant throughout each of the simulations in order to allow for isolation of the tidal impacts. The 31 days of modelled glacier evolution in each simulation span the month of August 2016 but, due to model design, are not a direct analogue for conditions during this period and should instead be viewed as diagnostic simulations.

The seven runs are summarised in Table 1. Simulation ALL serves as a control run and includes all identified tidal impacts (FM, CD, and SP), both calving mechanisms (surf and base), and frontal melt. By switching off selected mechanisms (see Sect. 3.2), six different simulations are designed to isolate the impacts of calving mechanisms (CM_{base}, CM_{surf}), tidal fluctuations (T_{SP}, T_{CD} , T_{FM}), and (absence of) frontal melt (NM).

For step V, post-processing, the occurrence of calving events was related to tidal cycles in a number of different ways. Firstly, the percentage of calving events occurring on rising or falling tides was calculated for both icebergs of all sizes and for large (> 500 m^3) icebergs. This threshold was chosen as it corresponds to 5 % of total icebergs. For these results, hypothesis testing (binomial distribution, one-tailed) was conducted with any results where $p < 0.05$ being considered statistically significant.

In addition, the water depth (deviance from mean sea level) at which calving events occurred was investigated to look for a pattern between e.g. low or high water levels and calving regardless of whether water levels are rising or falling. Finally, the occurrence of calving was also related to tidal amplitude (spring vs neap tides).

3.4 Observational data

Two profiles showing the frontal geometry of Kronebreen were mapped using a Kongsberg EM2040 multibeam (MB) echo-sounder and a Riegl VZ-6000 terrestrial LiDAR on the 24th August 2016 (see Fig. 3). Below the waterline, MB was used to get an image of the submarine morphology of the calving front. Above the waterline, LiDAR was instead used to image the calving front's geometry.

https://doi.org/10.5194/tc-2022-152
Preprint. Discussion started: 31 August 2022

Table 1. Summary of processes included in the suite of tidal simulations. Possible tidal impacts are SP (sea pressure), CD (crevasse depth), and FM (frontal melt) and are described in more detail in Sect. 3.2. The calving mechanisms 'surf' and 'base' are described in more detail in Sect. 3.3.

Simulation name	Tidal impact	Frontal melt	Calving mechanism
ALL	All	Y	surf and base
CM_{base}	All	Y	base
CM_{surf}	All	Y	surf
T_{SP}	SP	Y	surf and base
T_{CD}	CD	Y	surf and base
T_{FM}	FM	Y	surf and base
NM	All	N	surf and base

The Riegl VZ-6000 LiDAR is equipped with a long-range near-infrared laser and uses the time-of-flight principle to calculate a distance to the measured object. For the Kronebreen subareal ice cliff survey, the pulse repetition rate (PRR) was set to 50 kHz, and the horizontal and vertical angular resolutions at 0.0045°, resulting in a nominal spatial resolution of c. 5 cm at the distance of 1.5 km. However, due to unfavourable meteorological conditions, the survey geometry, and poor reflection from the ice cliff, the effective resolution was limited to c. 80 cm in horizontal direction and approx. 30 cm in the vertical. The instrument has a nominal distance accuracy of 10 mm and precision of 15 mm at a range of 150 m. The lowermost part of the cliff, in constant contact with wave action and water spray, has very low reflectivity in the near infrared part of the spectrum, and therefore no laser return was obtained at the waterline. Overall, based on previously published surveys of the ice cliffs, we conservatively estimate the measurement uncertainty at 30 cm.

The Kongsberg EM2040 multibeam echosounder is a wide band, high resolution shallow water mutibeam echosounder with one 0.4° wide transmit beam and 256 0.7° wide receiver beams. The instrument was mounted on a small 15 m research vessel and operated at a frequency of 200 kHz. Sampling frequency varied between 5 and 10 Hz and was limited by water depth. The range resolution was usually within 1 to 2 cm. The EM2040 was coupled with Kongsberg's Seapath 330+ Global Navigation and Satellite System (GNSS) positioning and Motion Reference Units (MRU). In additoin, positioning was aided by a local Real Time Kinematic (RTK) reference station placed on a nearby coastal area. As a result, positioning accuracy was better than 10 cm.

The two profiles, one shown in green and one in orange, consist of 1211 and 1006 points respectively, with both transects running from Easting 448000 to 448060 (UTM zone 33N). Soundings were taken between Northings 8756133 and 8756134 (green profile) and Northings 8756633 and 8756634 (orange profile). These data allow for comparison of undercut sizes between the model and observations but, due to the conceptual nature of the model, smaller scale morphologies cannot be compared. The green profile corresponds to the location of a subglacial plume, as identified from satellite imagery. The orange profile does not correspond to a satellite-identified plume location.

https://doi.org/10.5194/tc-2022-152
Preprint. Discussion started: 31 August 2022

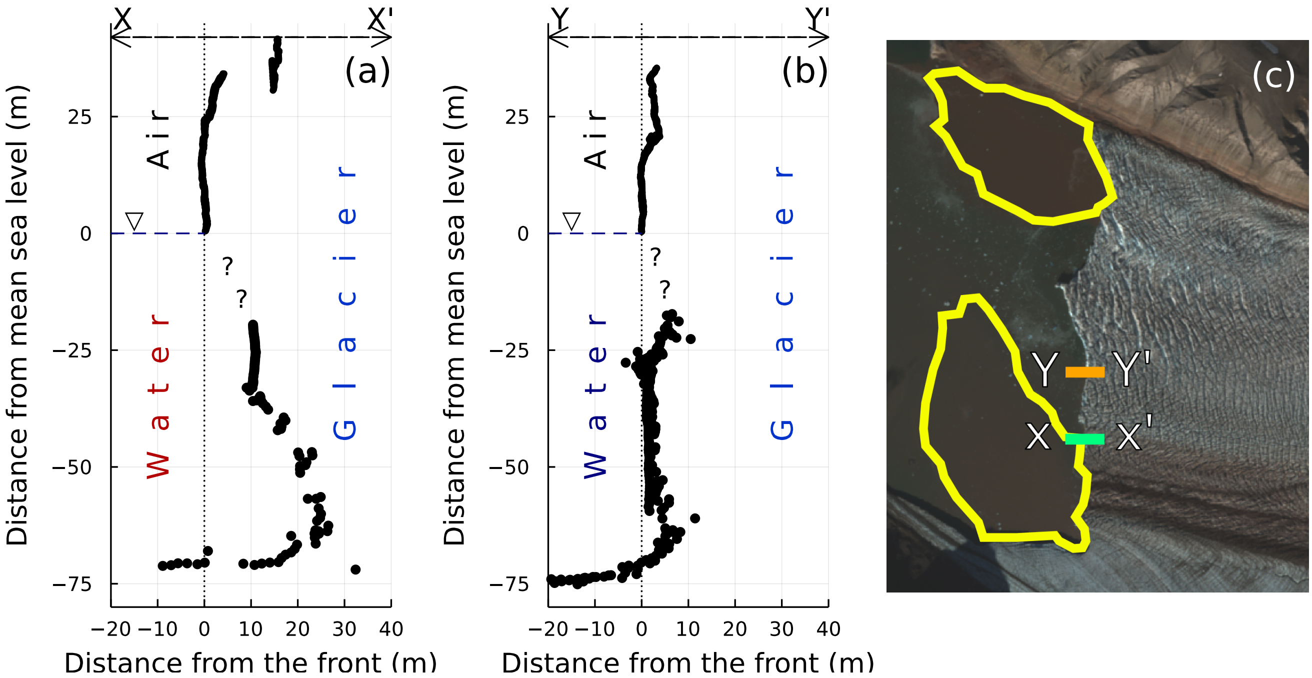

Figure 3. Panel (a): Frontal geometry at the X - X' (green) profile of Kronebreen as observed from MB and LiDAR data at the location denoted by the green line on Panel (c). Panel (b): Frontal geometry at the Y - Y' (orange) profile of Kronebreen as observed from MB and LiDAR data at the location denoted by the orange line on Panel (c). Panel (c) shows the location of the two profiles, as well as of the subglacial plumes identified from satellite imagery (yellow polygons). The background for Panel (c) is from the 22nd August 2016, two days before the MB/LiDAR data was collected. The background image is Copernicus Sentinel data (2022), retrieved from Copernicus Open Access Hub 23/05/2022, processed by ESA.

4 Results

For all seven main simulations (Table 1), the percentage of calving events occurring on a rising tide and a falling tide are shown in Table 2, with separate values for all icebergs and for large icebergs. Percentages are used to quantify the occurrences because the absolute number of calving events differs between simulations. The mean number of calving events in all seven simulations was 1915, corresponding to an average of 61 events per day or 2.6 events per hour. It can be seen that, when considering icebergs of all size, there is no clear preference for calving on a particular tidal phase. However, when focusing on large icebergs, a clear tidal signal can be seen in all the simulations. Specifically, ALL, CM_{base}, and NM show a preference for a rising tide whereas CM_{surf}, T_{SP}, T_{CD}, and T_{FM} show a preference for a falling tide.

4.1 Calving mechanisms

The CM_{surf} and CM_{base} simulations provide insight into how tidal fluctuations may have differential impacts on calving occurring from different calving mechanisms.

https://doi.org/10.5194/tc-2022-152
Preprint. Discussion started: 31 August 2022

Table 2. Percentage of calving events occurring during different tidal phases in each simulation. The percentages from some simulations (T_{CD} and NM, all icebergs) only add up to 99 because some calving events occurred when the gradient of the tide was exactly 0.0, thus preventing categorisation of the calving event as occurring on either a rising or falling tide. The percentage of time steps corresponding to a rising tide and a falling tides were both 50 %. Results which are statistically significant ($p < 0.05$) are presented in bold.

	All icebergs		Large icebergs	
Simulation name	% Falling tide	% Rising tide	% Falling tide	% Rising tide
ALL	49	51	42	58
CM_{base}	51	49	46	54
CM_{surf}	51	49	**68**	**32**
T_{SP}	50	50	56	44
T_{CD}	**48**	**51**	58	42
T_{FM}	**53**	**47**	**65**	**35**
NM	51	48	44	56

When considering the percentage of all calving events occurring on a falling and rising tide (Table 2), both the CM_{surf} and CM_{base} simulations show a very small preference for calving on a falling tide. However, when only large icebergs are considered, a strong and statistically significant preference for calving on a falling tide is seen for the CM_{surf} simulation whilst a small preference for calving on a rising tide is shown by the CM_{base} simulation. A greater percentage of icebergs in CM_{surf} were considered large than in CM_{base} (40 % compared to 5%, respectively), but the overall mass loss /margin change in the two simulations was similar due to significantly fewer CM_{surf} calvings as is shown in Fig. 4. In panels b and c of Fig. 4, the relation between calving events and tidal water level is shown. These panels show the deviance from mean sea level at which all calving events occurred during the CM_{surf} and CM_{base} simulations, as well as whether they occur on a rising or falling tide. It is clear that calving events from CM_{surf} preferentially occur when water levels are higher, whereas no such pattern is found for CM_{base}. Even when just considering large icebergs, CM_{surf} calving events still preferentially occur when water levels are high but, in addition, predominantly take place when the tide is falling. The calving events for both simulations occur, for the most part, in the same areas. However, there are two areas where CM_{base} events cluster but where CM_{surf} are rare. These areas correspond to the approximate locations of the sub-glacial plumes, which are denoted by the yellow ovals in Fig. 4a.

4.2 Impact of tides on calving

The occurrence of calving events from the simulations isolating tidal impacts (T_{SP}, T_{FM}, and T_{CD}) during rising and falling tides are summarised in Table 2. When considering calvings of all sizes, T_{FM} shows a statistically significant inclination to calve preferentially on a falling tide. In contrast, both T_{CD} and T_{SP} do not show a preference for any tidal phase. However,

https://doi.org/10.5194/tc-2022-152
Preprint. Discussion started: 31 August 2022

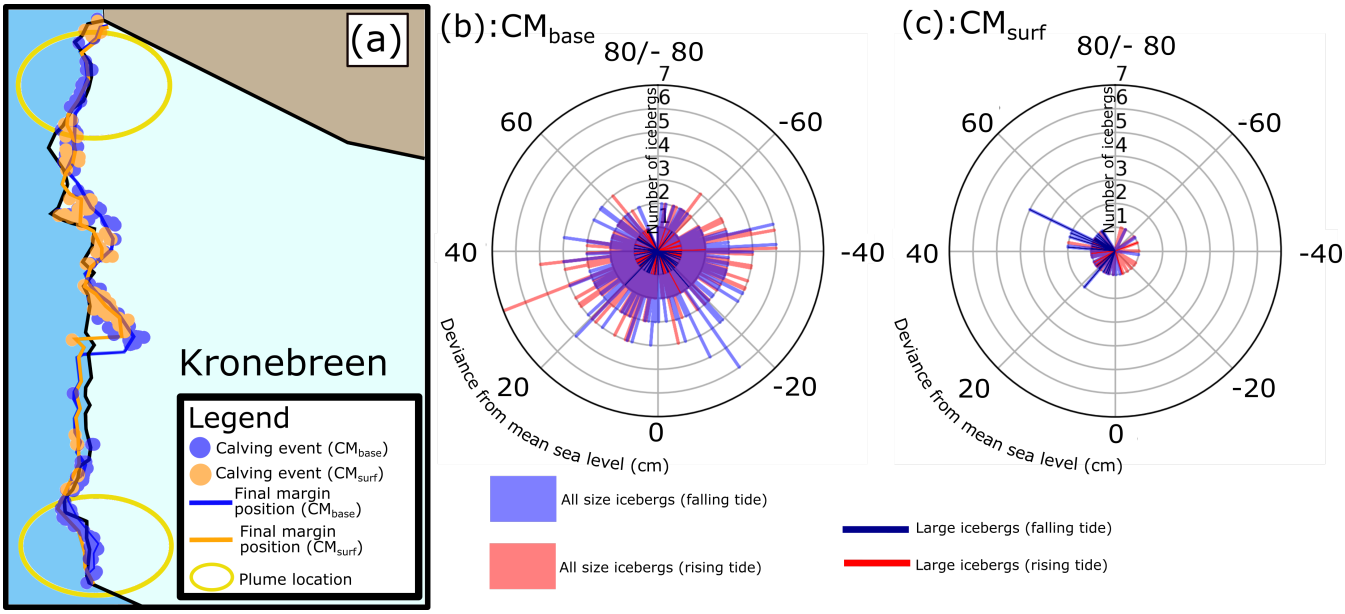

Figure 4. Figure comparing the results from the CM_{base} and CM_{surf} simulations. Panel (a): Location of calving events in CM_{surf} (orange) and CM_{base} (blue) superimposed over the margin position from the beginning of the simulations (black), the end of CM_{surf} (orange) and the end of CM_{base} (blue). The location of the plumes are indicated by the yellow ovals. Panels (b) and (c): All size calving events (thick transparent lines) and large calving events (thick opaque lines) plotted with regards to the water depth at which they occurred. The length of the line denotes the number of icebergs at a given water depth (to a precision of 0.1 cm) and the colour of the line denotes whether the calving event occurred on a rising or falling tide. Panel (b) shows results from CM_{base} and Panel (c) shows results from CM_{surf} where significantly fewer calving events were modelled.

the large icebergs from all three simulations (corresponding to 5 % of the total icebergs) showed a preference for calving on a falling tide, with the T_{FM} simulation showing the strongest and only statistically significant signal.

The relation between calving events and water depth (deviance from mean sea level) can reveal a more complex picture than can be garnered from considering the percentage of events occurring during different tidal phases. Instead, these data reveal if there is a relation between when calving occurs and absolute water levels (high or low) without consideration of the tidal phase. In Fig. 5c, data from T_{CD} is shown. Close inspection of these results shows that large calving events in the T_{CD} simulation tend to cluster around both high and low tides. No such relation was found between water depth and calving for the T_{SP} and T_{FM} simulations or for the T_{CD} simulation and all size icebergs.

4.3 Impacts of frontal melt on calving

In the NM simulation, which is the only simulation without frontal melt included, a slight preference for calving on a falling tide is shown when considering all icebergs and a larger preference is shown for calving on a rising tide when considering large icebergs (see Table 2 and Fig. 5). In terms of temporal trends, calving frequency is low in the first third of the simulation until

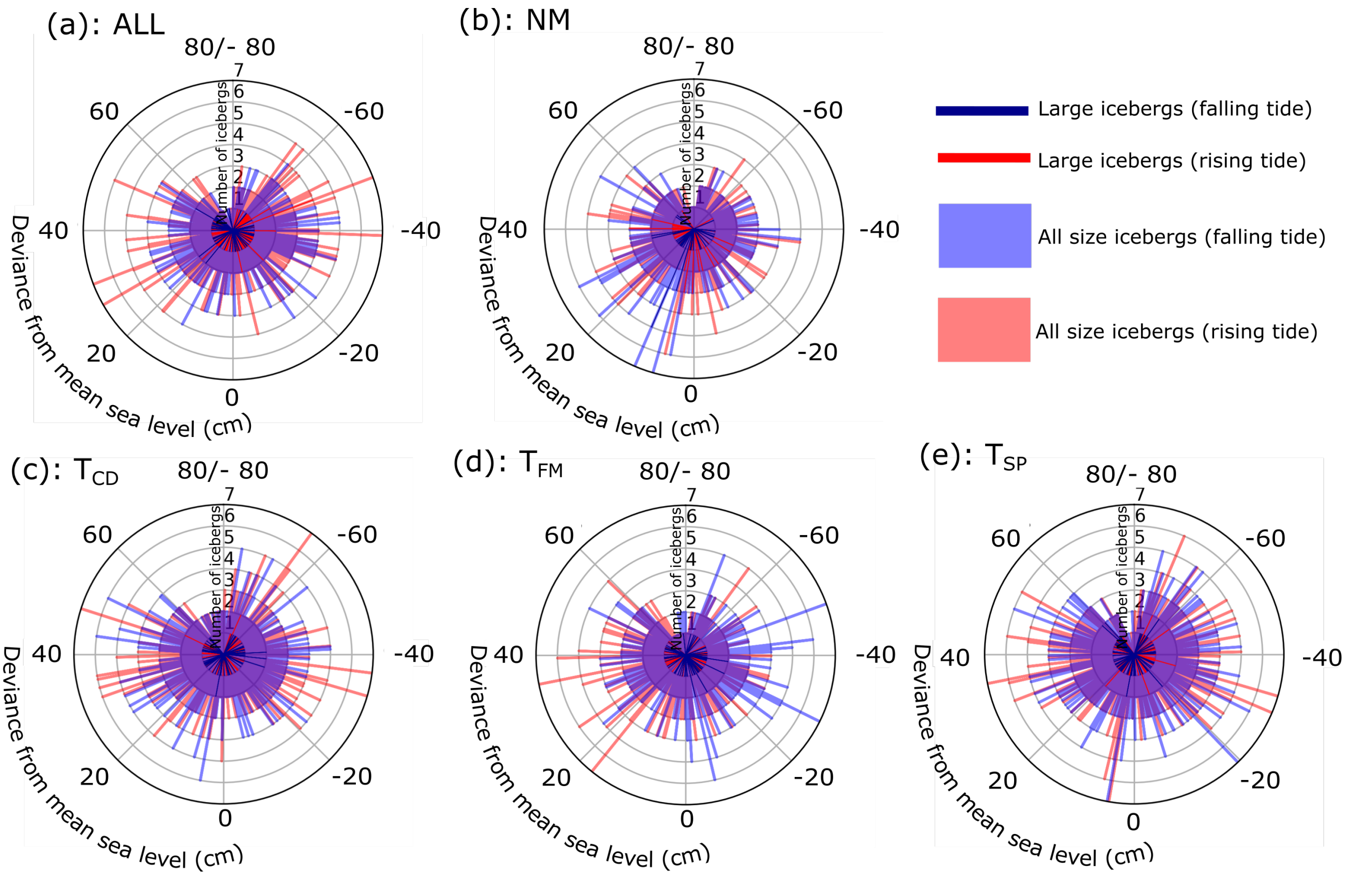

Figure 5. All size calving events (thick transparent lines) and large calving events (thin opaque lines) plotted with regards to the water depth at which they occurred. The length of the line denotes the number of icebergs at a given water depth and the colour of the line denotes whether the calving event occurred on a rising or falling tide. The water depth is plotted to a precision of 0.1 cm, making the iceberg count at each depth low (< 7) but cumulatively the many lines add up to over 1000. Panel (a) shows results from ALL, Panel (b) from NM, Panel (c) from T_{CD}, Panel (d) from T_{FM}, and Panel (e) from T_{SP}.

the 7th August, before picking up. Low calving frequencies are seen once more during the first neap tide (11th to 15th August), after which they increase again as the tidal amplitude increases.

This is in contrast to CM_{surf}, where a low calving frequency is seen throughout (Fig. 4). In addition, this is in contrast to all other simulations, where the general temporal trend is that calving frequency is initially high, after which a period of relative stability ensues. Around the middle of the simulation, calving activity picks up once again (an example from the T_{SP} simulation is shown in Fig. 6). The NM simulation has some similarities to these other simulations, but is distinct due the the earlier onset of increased calving frequency and the correlation with tidal amplitude.

The increase in calving frequency in all simulations except NM coincides with the development of a well-defined (c. 20 m) melt-driven undercut at the terminus, as can be seen in Fig. 7. The size of this modelled undercut varies throughout the

https://doi.org/10.5194/tc-2022-152
Preprint. Discussion started: 31 August 2022

The Cryosphere Discussions

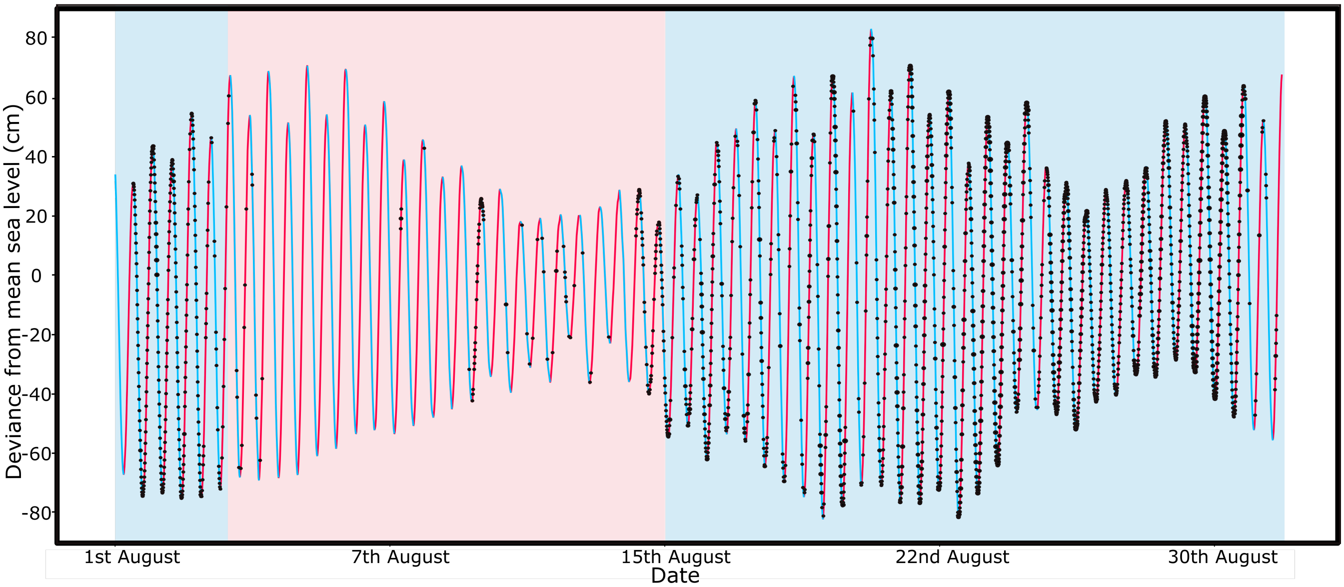

Figure 6. Changes in water depth due to tides during August 2016, with rising tides shown as red lines and falling tides as blue lines. Calving events from the SP simulation are denoted by black dots. The red shaded area denotes the period from the 15th - 31st August when calving activity is generally higher, whilst the blue shaded areas denote lower calving frequencies. Neap tides can be seen between 11th and 15th August as well as between 26th and 30th August.

simulations, with calving events leading to periodic reductions in size as part of the overhanging ice is removed. Modelled undercut sizes also vary spatially due to the differences in frontal melt rates across the calving front (Fig. 7). These spatial differences are also seen in the observational data, where an undercut of c. 25 m is observed near a plume compared to only c. 10 m in a non-plume area (see Fig. 3) The undercut size at which the modelled uptick in calving frequency occurs is similar in size to the c. 25 m undercut seen in the green (X to X') observational profile.

When focusing on the observed calving front morphology (Fig. 3), many small scale geometries can be seen. In particular, both observed profiles show an undercut between the waterline and -20 m after which a straight front is seen. For the Northern (orange) profile this straight front lasts for c. 40 m whereas for the Southern (green) profile this only lasts for c. 10 m. Near the bottom of the ice cliff, both profiles show another undercut.

5 Discussions

The results from the modelling experiments suggest that tidal cycles have a impact on calving frequency, but that the strength of the relationship is variable (cf. Table 2). The CM_{base} simulation has one of the weaker tidal signals and results from this simulation are not statistically significant, suggesting that calving events which occur due to the propagation of basal crevasses are primarily controlled by something other than water level fluctuations. On the other hand, large calving events in CM_{surf}

https://doi.org/10.5194/tc-2022-152
Preprint. Discussion started: 31 August 2022

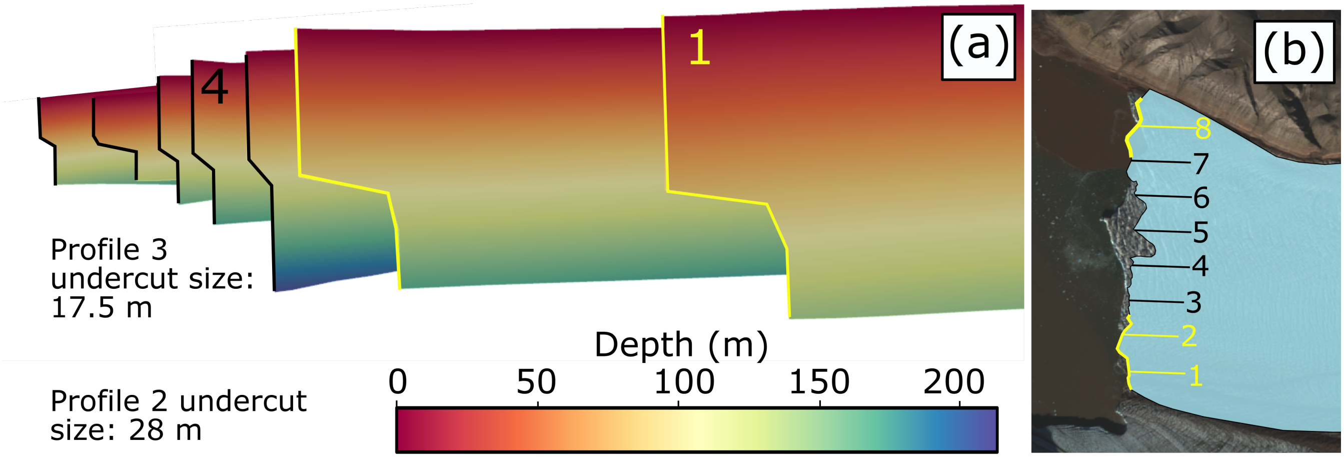

Figure 7. Panel (a): Undercut profiles from several locations normal to the orientation of the calving front of Kronebreen as denoted by the lines and numbers in panel (b). Profile number 8 cannot be seen due to the curvature of the glacier terminus. Yellow lines indicate plume locations. The profiles show the modelled frontal morphology from the midpoint of the CM_{surf} simulation. Profile numbers 2 and 3 correspond to the location of the green and orange profiles in Fig. 3 respectively. Panel (b): Modelled glacier outline from the midpoint of the CM_{surf} simulation, with the location of the profiles (numbered lines) and plumes (yellow areas) shown. Background image for panel B is Copernicus Sentinel data (2022), retrieved from Copernicus Open Access Hub 23/05/2022, processed by ESA.

show a strong and statistically significant tidal signal and, even when considering all size calvings, a relationship is seen with water depth (Fig. 4). For results that are not statistically significant (Table 2), there is not enough evidence at the 95% confidence level to state that the distribution of calving events between tidal phases is unlikely to occur by chance but it does not mean that there is no connection between tidal cycles and calving.

When considering tidal impacts, a preference for the calving of large icebergs to occur on a falling tide was shown in the T_{SP}, T_{FM}, and T_{CD} simulations (Table 2 and Sect. 4.2). In terms of T_{SP}, a falling tide can promote calving by causing a reduction in the amount of back (sea) pressure exerted on the calving front. This mechanism has been invoked before with regards to tides and calving, for instance at Tunabreen, Svalbard (How et al., 2019). Here, the authors conducted a time lapse study and found that 68 % of calving events occurred on a falling tide. Changes in the water level during the study period led to a 2 % reduction in back stress during low tide, with this small change being sufficient to cause increased numbers of calving events (How et al., 2019). Another observational study found similar results, with large calvings at Yahtse glacier, Alaska, being significantly more likely during low or falling tides than during high or rising tides (Bartholomaus et al., 2015). Once again, this pattern was attributed to the increased backstress exerted on the glacier by the water during high/ rising tides. This study additionally found that the impact of tides was only clear for large icebergs (Bartholomaus et al., 2015), something which is corroborated by our modelling study.

Previous work at Store glacier, Greenland, found that basal crevasse propagation was much higher across parts of the glacier front which were floating (Todd et al., 2019). At Store glacier, buoyancy forces acting on the floating parts of the terminus were seen to promote basal crevassing and subsequent calving, often in conjunction with changes in the stress regime as precipitated by melt undercutting (Todd et al., 2019). This links to the T_{FM} simulation, where the proposed mechanism for more frequent calving on the falling tide is that frontal melt accumulates during both the rising and falling tides, leading to the largest undercuts occurring during the falling tide. When the undercuts are largest, there is also the greatest propensity for calving via the promotion of basal crevassing, leading to increased calving on a falling tide. Given that large calving events from the T_{FM} simulation showed one of the strongest tidal signals, combined with the fact that both all size calving and large calving statistics from T_{FM} were significant, it appears that melt driven undercutting has a particularly strong impact on calving patterns at Kronebreen. The T_{CD} simulation is more complex, as a high or rising water level should make it easier for calving via the propagation of surface crevasses to occur. This is the case for all size calvings where, although the percentage difference is small, the pattern is statistically significant. Large calvings instead preferentially occur on a falling tide and this could be due to the dominance of the basal calving mechanism, leading to a subdued signal from the increased crevasse water depth. The results displayed in Fig. 5c show that large calving events tend to cluster around either high or low tides, which could point to two different mechanisms at play. Calving events which occur at high tide may be related to the propagation of surface crevasses, preferentially occurring when water levels are higher. However, the more numerous calving events occurring due to basal crevassing may instead preferentially occur at low tide and confuse the tidal signal. The influence of water level in surface crevasses in our simulations was not as strong as found in previous studies such as that by Cook et al. (2012), where the amount of water in surface crevasses was varied to look at the impact on calving. In the Cook et al. study, the presence of increased water in crevasses led to a large increase in calving; an additional few metres of water caused the glacier to switch to a retreat of 1.9 km yr^{-1} from an advance of 3.5 km yr^{-1}. It is important to note that this does not explicitly model tidal cycles, but instead just considers the influence of water in crevasses.

In the absence of frontal melt, the NM simulation shows increased large iceberg calving during rising tides. We suggest that, in the absence of an undercut, calving events at Kronebreen are predominantly caused by surface crevasse propagation. In this scenario, a high or rising water level makes it easier for these surface crevasses to reach the waterline. There is also some indication that tidal amplitude is important for calving in NM, as calving frequency drops during the first neap tide before picking back up again as the tidal amplitude increases (see Sect. 4.3 and tidal cycles in Fig. 6). This could be due to the fact that, when tidal amplitudes are higher, the distance that a surface crevasse must propogate to reach water level is at a minimum. However, during the second neap tide the reduction in calving frequency is less defined, suggesting a complex relationship. This type of nuanced pattern has also been identified by observations at LeConte glacier, Alaska, where calving was correlated to the amplitude of tidal cycles (O'Neel et al., 2003). As with our data, evidence was found for increased calving during spring tides (O'Neel et al., 2003).

When considering the calving mechanisms separately, a clear preference for large calvings to occur on a falling tide is seen in the CM_{surf} simulation. This suggests that the combined influence of reduced sea pressure and accumulated frontal melt outweigh the pro-calving effect of rising water levels in crevasses. However, calving events in this simulation also cluster around parts of the tidal cycle when water levels are high (see Fig. 4). This could suggest that high water levels prime the glacier for calving by making it easier for surface crevasses to reach the waterline, but that these calving events are then triggered by the falling tide due to, for example, a reduction in back pressure on the terminus. The CM_{base} simulation instead shows a slight preference for calving on a rising tide, with this potentially being linked to increased buoyancy forces on a rising tide. However, this preference is not as clear as for other simulations and is likely an artefact of the model.

In the ALL simulation, with all calving mechanisms and tidal impacts included, a preference is seen for large icebergs to calve on a rising tide. However, there is no clear preference for all sizes of icebergs. This is similar to the results of CM_{base}, which could be related to the fact that a large number of calving events at Kronebreen occur due to the propagation of basal crevasses. None of the ALL results were statistically significant, suggesting that when all the tidal impacts and calving mechanisms are combined, there is no clear preference for a specific tidal phase.

The modelled undercut grows during the length of the simulations, and a key question is whether the modelled undercut is realistic. The observational MB/LiDAR data shows that undercut size at Kronebreen can be around 25 m at plume locations and around 10 m at non-plume locations (see Fig. 3). The modelled plume undercut at the midpoint of the simulations corresponds well to the size of the observed plume undercut, with this being the time point at which calving frequency tends to increase in the model (Fig. 7). At non-plume locations, the model overestimates undercut size (17.5 m compared to 10 m). This suggests that the assertion of melt undercutting being a key driver of calving processes at Kronebreen is somewhat justified, at least at the locations of subglacial plumes. However, the observations only show two profiles from across the glacier front, taken at a single point in time. It is thus not clear how variable the undercut size can be, either temporally or spatially. Previous studies have found evidence for large spatial variability in undercut sizes at other glaciers, making it likely that that the same holds true for Kronebreen (Fried et al., 2015; Rignot et al., 2015). The modelled undercut reaches a mean of c. 40 m in size by the end of the simulations, which is likely larger than reality. However, we do not observe any further changes in calving patterns as the undercut continues to grow and so this potential overestimation is unlikely to have had a large impact on the results. It must be noted that the pattern of frontal melt implemented in this study is not necessarily realistic, but was chosen in order to allow isolation of the impacts of tidal fluctuations as well as to allow for investigation of how changing undercut sizes lead to changes in calving patterns. Our modelled undercuts are generally smaller than those modelled by Vallot et al. (2018). Here, undercuts at Kronebreen were also modelled using Elmer and sizes of up to c. 150 m were found for a high discharge plume area and up to c. 40 m for a low discharge plume area (Vallot et al., 2018). The authors of this paper note that the undercuts were allowed to develop with no calving implemented, which likely makes them overestimates. Further work is thus needed to better understand the frontal morphology of Kronebreen and its impacts for calving patterns. Despite this, the MB/LiDAR data presented here suggests that frontal melt is significant at Kronebreen, agreeing with previous studies and adding weight to the argument that frontal melt exerts a first order control its calving dynamics (Luckman et al., 2015; Holmes et al., 2019).

At Kronebreen, we propose that a similar mechanism to that described by Todd et al. (2019) for Store glacier is at play. At Kronebreen, the development of a well defined undercut of around 20 m is suggested to lead to accelerated basal crevassing and calving. Evidence for this comes from the fact that the calving frequency in all of the simulations except for CM_{surf} and NM increases in the latter half of the simulation once the undercut has reached this critical size. In addition, calving during the CM_{base} simulation increasingly clusters around plume locations as time goes on, where the modelled undercuts are largest

https://doi.org/10.5194/tc-2022-152
Preprint. Discussion started: 31 August 2022

(Fig. 6 and Sect. 4.1). A greater proportion of calving events occurring due to basal crevasse propagation were considered small than events occurring from surface crevasse propagation. This suggests that the smaller, more frequent calving events at Kronebreen are primarily controlled by undercut development and may be independent of tidal fluctuations.

The results presented above suggest that, in settings with little to no undercut, high water levels may be associated with increased calving frequency as surface crevasse driven calving dominates. However, in settings with larger undercuts, falling or low tides are likely to preferentially promote calving. This may lead to differing and sometimes contrasting patterns at different glaciers, as well as between different areas on the same glacier due to, for example, the location of subglacial plumes. Seasonal and inter-annual variations in the level of frontal melt may also lead to corresponding variations in the relationship between tidal fluctuations and calving.

The majority of previous studies have found that calving occurs preferentially on low or falling tides, which does not hold true for all the data presented here. This is likely in part due to site specific characteristics of different glaciers but may also be related to bias in both observations and model-derived data sets. Specifically, the modelled calving events in this study were generally reasonably small (< 500 m^3) when compared to previous observational studies of Kronebreen's calving behaviour such as by Köhler et al. (2019). This is likely partly due to observational records preferentially identifying larger calving events, but also suggests that the model presented here overestimates the number of small calving events. As larger calving events exhibit a stronger tidal signal, this may cause our modelling study to underestimate tidal influence whilst at the same time suggesting that observational studies overestimate tidal influence. Further study focusing on comparison of modelled and observational calving sizes would be fruitful to better constrain iceberg sizes at Kronebreen.

It must be additionally noted that, in our model, water level in crevasses is assumed to be in equilibrium with tidal water level. However, it is possible that this does not hold true and that there is instead a delay in the connection between the fjord and crevasse water levels. This is an important factor to consider; a previous study looking at calving found that crevasse opening is greatest at low tides (Van Dongen et al., 2020). However, this relationship is complex; it was the difference in water level between the crevasse and ocean that was most important, with maximum opening rates occurring when this difference was at least 4 m, as can occur when there is a delay in water drainage between the glacier and ocean (Van Dongen et al., 2020). Thus, further observational studies to determine how water levels in crevasses at Kronebreen vary is important for better constraining the influence of tides.

Both tidal cycles and individual calving events occur on short timescales and, as such, are related to both viscous and elastic deformation (e.g. Reeh et al. (2003)). However, in the model set-up described here, a viscous model was used which does not include elastic deformation. This approach was chosen as it allowed for a whole month of tidal cycles to be investigated which would not have been possible with a more expensive visco-elastic model. The implication of this model choice is that the results should be interpreted with regards to the broad patterns displayed, rather than by considering the individual calving events themselves.

https://doi.org/10.5194/tc-2022-152
Preprint. Discussion started: 31 August 2022

Other simplifications were used for the model in order to allow for the isolation of the tidal impacts. For example, no SMB was prescribed and frontal melt rates were kept constant during the course of the simulation. Consideration of the observed profiles of Kronebreen's frontal geometry (Fig. 3) show that the calving front morphology is, in reality, complex. The presence of an undercut just below the waterline at around -20 m is likely due to warm waters, with sound velocity profiles presented by Holmes et al. (2019) showing that the warmest waters (c. 6 ^{o} C) during mid August 2016 were located at or around a depth of 20 m. The undercuts near the base of the profiles are instead likely a consequence of sub-glacial discharge, with a more more pronounced undercut on the Southern (green) profile where a subglacial plume can be identified on satellite imagery. Incorporation of these more nuanced frontal melt patterns would be beneficial for further understanding the controls on calving at Kronebreen, and for running simulations to investigate the impact of calving events of glacier dynamics similarly to e.g. Amundson et al. (2022).

Although the tidal cycles and simulation set-up was configured to correspond to August 2016, the model simplifications described up mean that the experiments are best viewed as diagnostic simulations which investigate the roles of tides and undercutting with regards to calving, rather than as a perfect analogue to August 2016.

6 Conclusions

Tidal impacts on calving at Kronebreen are complex, with a clear relationship only being seen when certain calving mechanisms or tidal impacts are considered. The majority of statistically significant results show that calving is more likely on a falling tide, due to the combined impacts of reduced back pressure and accumulated frontal melt. However, the development of a melt derived undercut of c. 20 m leads to the increased propagation of basal crevasses and an increased frequency of calving events which do not show a tidal signal. This suggests that, when undercuts reach a critical size, their presence exerts a first order control on calving patterns at Kronebreen. During these periods, tidal fluctuations constitute only a second order control on calving dynamics. These findings suggest that frontal melt is of great importance for frontal ablation at Kronebreen, and provide motivation for investigating further the complex frontal morphology of Kronebreen and the extent to which undercut sizes vary both spatially and temporally. In addition, further modelling experiments which utilise more realistic frontal melt scenarios and look into the longer-term development of Kronebreen (and other glaciers) are needed in order to better understand the combined impacts of frontal melt and surface mass balance for both the frontal ablation and overall dynamics/ mass balance of the glacier.

https://doi.org/10.5194/tc-2022-152
Preprint. Discussion started: 31 August 2022

415 **Appendix A**

A1 Results related to stages I to III, from inversion for basal friction to relaxed, spun-up state of Kronebreen

The Robin inverse method aims to minimise a cost function that measures the mismatch between modelled and observed velocities, and is described in more detail by e.g. Gillet-Chaulet et al. (2012). A regularisation parameter, λ, is tuned in order to find the best compromise between the smoothness of the inverted field and the minimisation of the cost function. The parameter λ is chosen by creating an L-curve (Fig. A1) and choosing the value at the base of the 'L' (Hansen, 2001). The L-curve plots J_{reg} (smoothness of the inverted field) against J_O (mismatch between the model and observations). The chosen value of λ in this study, $5.0e09$, ensures that the misfit between the modelled and observed velocities remain small whilst not causing too much smoothing of the basal friction field. The inverted summer basal friction field used for the suite of main simulations is shown in Fig. A2 Panel (a). Here, lower friction values can be seen across the southern edge of Kronebreen which is a similar pattern to that found by Vallot et al. (2018) during summer 2013.

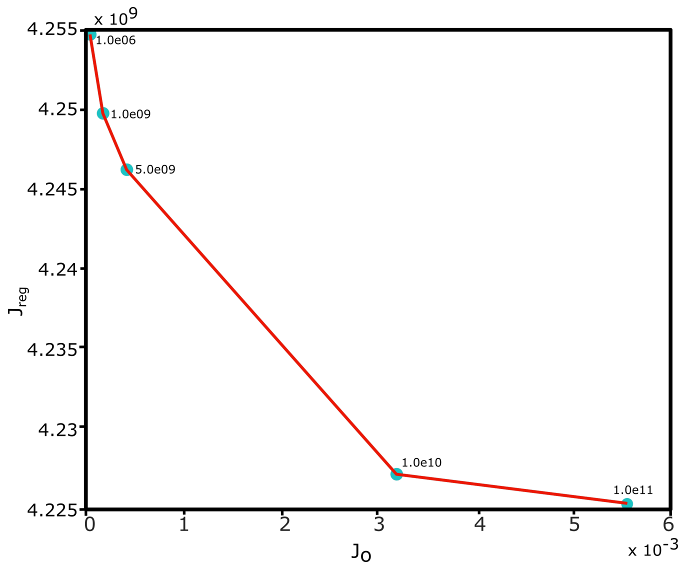

Figure A1. L curve from the summer inversion, with the λ values shown next to the data points. The chosen value for λ is 5.0e09. The x axis shows J_O (mismatch between the model and observations) and the y axis shows J_{reg} (variable smoothness).

The modelled summer velocities at the end of stage I (inversion) are shown in Fig. A2 panel (b), with frontal velocities reaching up to 750 m yr^{-1} (2.05 m d^{-1}). This corresponds well to observed velocities from the summer of 2016, where mean frontal velocities reached highs of c. 2 m d^{-1} (Holmes et al., 2019). At the end of stage II (spin-up), velocities show a similar maximum magnitude but extend over a greater proportion of the terminus area (see Fig. A2 panel (c)). The mean frontal velocities from the area denoted by the black polygon in Fig. A2 panel (c) are shown in Fig. A3. Note that, even in a steady state, seasonal variations in velocity are seen as a result of varying temperature forcing and basal friction (Fig. A3). The

https://doi.org/10.5194/tc-2022-152
Preprint. Discussion started: 31 August 2022

position of the calving front changes during stage III (relaxation) with the change in frontal and surface geometries occurring synchronously with a slowdown in velocity (Fig. A2 panel (d)). The frontal velocities instead lie around 1.8 - 1.9 m d^{-1}, which remains within the range of summer 2016 velocities observed at Kronebreen (Holmes et al., 2019). The results shown in Fig. A2 panel (d) correspond to the initial conditions for all simulations in stage IV.

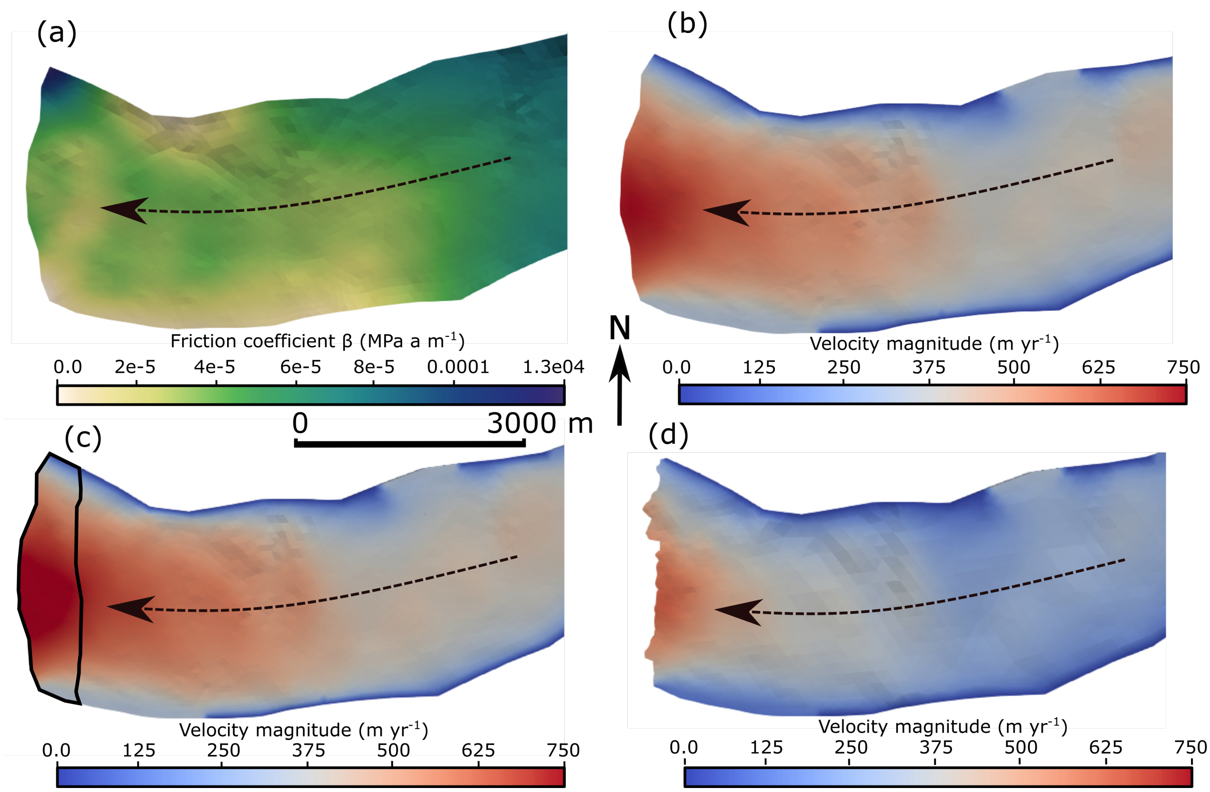

Figure A2. Results from steps I to III of the simulation workflow for the frontal portion of Kronebreen. In all panels, the dotted lines shown the flow direction. Panel (a): Inverted summer basal friction at Kronebreen. Panel (b): Modelled summer velocities at Kronebreen at the end of stage I (inversion). Panel (c): Modelled summer velocities at Kronebreen at the end of stage II (spin-up), with the black polygon denoting the area over which mean velocity values were calculated for plotting in Fig. A3. Panel (d): Modelled summer velocities and margin position at the end of stage II (relaxation).

https://doi.org/10.5194/tc-2022-152
Preprint. Discussion started: 31 August 2022

The Cryosphere Discussions

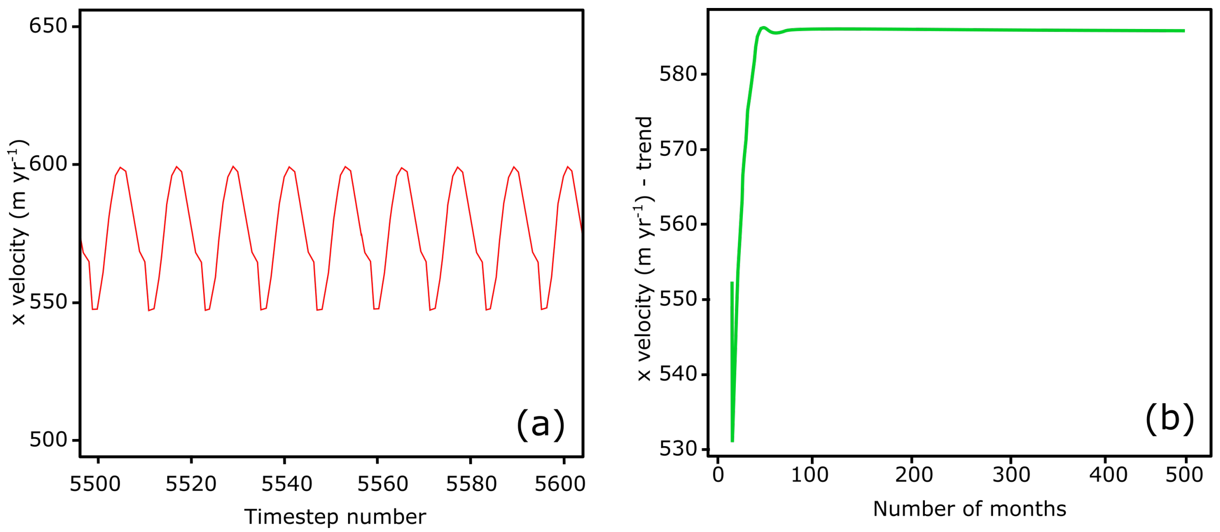

Figure A3. Example results from the spin-up showing mean frontal velocities in the x direction (positive denoting flow towards the glacier terminus). The frontal area from where mean velocities are calculated is shown by the black polygon in Fig. A2 Panel (c). Panel (a): A close up of the x-velocity time series from the spin-up simulation, with clear seasonal variation visible. The nine peaks in the figure correspond to nine subsequent summer velocity maxima. Panel (b): The decomposed trend of the x velocities from the spin-up. By the end of the spin-up, there is no directional trend, thus showing the velocities to have converged.

Code and data availability. The code for the Elmer/Ice model is available at github.com/ElmerCSC/elmerfem. The Multibeam and LiDAR data used for the frontal profile of Kronebreen is available from the Bolin Centre for Climate Research's database (https://doi.org/10.17043/noormets-2022-kronebreen-1). The tidal data used is available from kartverket.no. The SMB data used for the model spin-up is available online at https://doi.pangaea.de/10.1594/PANGAEA.920984.

Author contributions. FAH designed the study, with the help of NK and EvD. FAH ran the simulations with assistance from EvD and NK. The multibeam data was collected by RN and NK, and the LiDAR data was collected by MP. FAH and NK wrote the manuscript, with the help of all authors.

Competing interests. The authors declare no competing interests.

Acknowledgements. The work was funded by the Swedish Research Council FORMAS under grants 214-2013-1600 and 2017- 00665 awarded to NK. The simulations were enabled by resources provided by the Swedish National Infrastructure for Computing (SNIC) at the National Supercomputer Centre (NSC) partially funded by the Swedish Research Council through grant agreement no. 2018-05973. The

https://doi.org/10.5194/tc-2022-152
Preprint. Discussion started: 31 August 2022

The Cryosphere Discussions

LiDAR and multibeam data was collected as part of the CalvingSEIS project, funded by the Research Council of Norway. The authors are grateful to Brice Noël for the daily SMB data used in the model spin-up.

References

Amundson, J. M., Truffer, M., and Zwinger, T.: Tidewater glacier response to individual calving events, Journal of Glaciology, pp. 1–10, https://doi.org/10.1017/JOG.2022.26, 2022.

Arthern, R. J. and Gudmundsson, G. H.: Initialization of ice-sheet forecasts viewed as an inverse Robin problem, Journal of Glaciology, 56, 527–533, https://doi.org/10.3189/002214310792447699, 2010.

Bartholomaus, T. C., Larsen, C. F., West, M. E., O'Neel, S., Pettit, E. C., and Truffer, M.: Tidal and seasonal variations in calving flux observed with passive seismology, Journal of Geophysical Research: Earth Surface, 120, 2318–2337, https://doi.org/10.1002/2015JF003641, 2015.

Benn, D. I., Warren, C. R., and Mottram, R. H.: Calving processes and the dynamics of calving glaciers, Earth-Science Reviews, 82, 143–179, https://doi.org/10.1016/J.EARSCIREV.2007.02.002, 2007.

Błaszczyk, M., Jania, J., and Res, J. H.: Tidewater glaciers of Svalbard: Recent changes and estimates of calving fluxes, Polish Polar Research, 30, 85–142, http://www.polish.polar.pan.pl/ppr30/PPR30-085.pdf, 2009.

Christoffersen, P., Mugford, R. I., Heywood, K. J., Joughin, I., Dowdeswell, J. A., Syvitski, J. P. M., Luckman, A., and Benham, T. J.: Warming of waters in an East Greenland fjord prior to glacier retreat: mechanisms and connection to large-scale atmospheric conditions, The Cryosphere, 5, 701–714, https://doi.org/10.5194/tc-5-701-2011, 2011.

Cokelet, E. D., Tervalon, N., and Bellingham, J. G.: Hydrography of the West Spitsbergen Current, Svalbard Branch: Autumn 2001, Journal of Geophysical Research, 113, C01 006, https://doi.org/10.1029/2007JC004150, 2008.

Cook, S., Zwinger, T., Rutt, I. C., O'Neel, S., and Murray, T.: Testing the effect of water in crevasses on a physically based calving model, Annals of Glaciology, 53, 90–96, https://doi.org/10.3189/2012AOG60A107, 2012.

Cottier, F., Tverberg, V., Inall, M., Svendsen, H., Nilsen, F., and Griffiths, C.: Water mass modification in an Arctic fjord through cross-shelf exchange: The seasonal hydrography of Kongsfjorden, Svalbard, J. Geophys. Res, 110, https://doi.org/10.1029/2004JC002757, 2005.

Deschamps-Berger, C., Nuth, C., Van Pelt, W., Berthier, E., Kohler, J., and Altena, B.: Closing the mass budget of a tidewater glacier: the example of Kronebreen, Svalbard, Journal of Glaciology, 65, 136–148, https://doi.org/10.1017/JOG.2018.98, 2019.

Dunse, T., Schuler, T. V., Hagen, J. O., and Reijmer, C. H.: Seasonal speed-up of two outlet glaciers of Austfonna, Svalbard, inferred from continuous GPS measurements, Cryosphere, 6, 453–466, https://doi.org/10.5194/TC-6-453-2012, 2012.

Enderlin, E. M., Howat, I. M., Jeong, S., Noh, M. J., Van Angelen, J. H., and Van Den Broeke, M. R.: An improved mass budget for the Greenland ice sheet, Geophysical Research Letters, 41, 866–872, https://doi.org/10.1002/2013GL059010, 2014.

Fried, M. J., Catania, G. A., Bartholomaus, T. C., Duncan, D., Davis, M., Stearns, L. A., Nash, J., Shroyer, E., and Sutherland, D.: Distributed subglacial discharge drives significant submarine melt at a Greenland tidewater glacier, Geophysical Research Letters, 42, 9328–9336, https://doi.org/10.1002/2015GL065806, 2015.

Gagliardini, O., Zwinger, T., Gillet-Chaulet, F., Durand, G., Favier, L., De Fleurian, B., Greve, R., Malinen, M., Martín, C., Råback, P., Ruokolainen, J., Sacchettini, M., Schäfer, M., Seddik, H., and Thies, J.: Capabilities and performance of Elmer/Ice, a new-generation ice sheet model, Geoscientific Model Development, 6, 1299–1318, https://doi.org/10.5194/GMD-6-1299-2013, 2013.

Gillet-Chaulet, F., Gagliardini, O., Seddik, H., Nodet, M., Durand, G., Ritz, C., Zwinger, T., Greve, R., and Vaughan, D. G.: Greenland ice sheet contribution to sea-level rise from a new-generation ice-sheet model, Cryosphere, 6, 1561–1576, https://doi.org/10.5194/TC-6-1561-2012, 2012.

Hansen, P. C.: The L-curve and its use in the numerical treatment of inverse problems, in: Computational inverse problems in electrocardiology, pp. 119–142, 2001.

https://doi.org/10.5194/tc-2022-152
Preprint. Discussion started: 31 August 2022

The Cryosphere Discussions
Open Access
EGU

Holland, D. M., Thomas, R. H., de Young, B., Ribergaard, M. H., and Lyberth, B.: Acceleration of Jakobshavn Isbræ triggered by warm subsurface ocean waters, Nature Geoscience, 1, 659–664, https://doi.org/10.1038/ngeo316, 2008.

Holmes, F. A., Kirchner, N., Kuttenkeuler, J., Krützfeldt, J., and Noormets, R.: Relating ocean temperatures to frontal ablation rates at Svalbard tidewater glaciers: Insights from glacier proximal datasets, Scientific Reports, 9, 9442, https://doi.org/10.1038/s41598-019-45077-3, 2019.

Holmes, F. A., Kirchner, N., Prakash, A., Stranne, C., Dijkstra, S., and Jakobsson, M.: Calving at Ryder Glacier, Northern Greenland, Journal of Geophysical Research: Earth Surface, 126, e2020JF005 872, https://doi.org/10.1029/2020JF005872, 2021.

How, P., Schild, K. M., Benn, D. I., Noormets, R., Kirchner, N., Luckman, A., Vallot, D., Hulton, N. R. J., and Borstad, C.: Calving controlled by melt-under-cutting: detailed calving styles revealed through time-lapse observations, Annals of Glaciology, pp. 1–12, https://doi.org/10.1017/aog.2018.28, 2019.

IPCC: IPCC Special Report on the Ocean and Cryosphere in a Changing Climate, Intergovernmental Panel on Climate Change, 2019.

Jakobsson, M., Mayer, L. A., Nilsson, J., Stranne, C., Calder, B., O'Regan, M., Farrell, J. W., Cronin, T. M., Brüchert, V., Chawarski, J., Eriksson, B., Fredriksson, J., Gemery, L., Glueder, A., Holmes, F. A., Jerram, K., Kirchner, N., Mix, A., Muchowski, J., Prakash, A., Reilly, B., Thornton, B., Ulfsbo, A., Weidner, E., Åkesson, H., Handl, T., Ståhl, E., Boze, L.-G., Reed, S., West, G., and Padman, J.: Ryder Glacier in northwest Greenland is shielded from warm Atlantic water by a bathymetric sill, Communications Earth & Environment, 1, 1–10, https://doi.org/10.1038/s43247-020-00043-0, 2020.

Jenkins, A.: Convection-Driven Melting near the Grounding Lines of Ice Shelves and Tidewater Glaciers, Journal of Physical Oceanography, 41, 2279–2294, https://doi.org/10.1175/JPO-D-11-03.1, 2011.

Karlsson, N. B., Solgaard, A. M., Mankoff, K. D., Gillet-Chaulet, F., MacGregor, J. A., Box, J. E., Citterio, M., Colgan, W. T., Larsen, S. H., Kjeldsen, K. K., Korsgaard, N. J., Benn, D. I., Hewitt, I. J., and Fausto, R. S.: A first constraint on basal melt-water production of the Greenland ice sheet, Nature Communications, 12, 1–10, https://doi.org/10.1038/s41467-021-23739-z, 2021.

King, M. D., Howat, I. M., Candela, S. G., Noh, M. J., Jeong, S., Noël, B. P. Y., van den Broeke, M. R., Wouters, B., and Negrete, A.: Dynamic ice loss from the Greenland Ice Sheet driven by sustained glacier retreat, Communications Earth & Environment 2020 1:1, 1, 1–7, https://doi.org/10.1038/s43247-020-0001-2, 2020.

Köhler, A., Pętlicki, M., Lefeuvre, P.-M., Buscaino, G., Nuth, C., and Weidle, C.: Contribution of calving to frontal ablation quantified from seismic and hydroacoustic observations calibrated with lidar volume measurements, The Cryosphere, 13, 3117–3137, https://doi.org/10.5194/tc-13-3117-2019, 2019.

Le Clec'h, S., Quiquet, A., Charbit, S., Dumas, C., Kageyama, M., and Ritz, C.: A rapidly converging initialisation method to simulate the present-day Greenland ice sheet using the GRISLI ice sheet model (version 1.3), Geoscientific Model Development, 12, 2481–2499, https://doi.org/10.5194/GMD-12-2481-2019, 2019.

Lindbäck, K., Kohler, J., Pettersson, R., Nuth, C., Langley, K., Messerli, A., Vallot, D., Matsuoka, K., and Brandt, O.: Subglacial topography, ice thickness, and bathymetry of Kongsfjorden, northwestern Svalbard, Earth System Science Data, 10, 1769–1781, https://doi.org/10.5194/ESSD-10-1769-2018, 2018.

Luckman, A., Benn, D. I., Cottier, F., Bevan, S., Nilsen, F., and Inall, M.: Calving rates at tidewater glaciers vary strongly with ocean temperature, Nature Communications, 6, 1–7, https://doi.org/10.1038/ncomms9566, 2015.

Nilsen, F., Cottier, F., Skogseth, R., and Mattsson, S.: Fjord–shelf exchanges controlled by ice and brine production: The interannual variation of Atlantic Water in Isfjorden, Svalbard, Continental Shelf Research, 28, 1838–1853, https://doi.org/10.1016/J.CSR.2008.04.015, 2008.

Noël, B. P. Y., Jakobs, C. L., van Pelt, W., Lhermitte, S., Wouters, B., Kohler, J., Hagen, J. O., Luks, B., Reijmer, C., van de Berg, W. J., and van den Broeke, M. R.: Annual surface mass balance (SMB) and components of Svalbard glaciers statistically downscaled to 500 m spatial resolution (1958-2018), https://doi.pangaea.de/10.1594/PANGAEA.920984, 2020.

O'Neel, S., Echelmeyer, K. A., and Motyka, R. J.: Short-term variations in calving of a tidewater glacier: LeConte Glacier, Alaska, U.S.A., Journal of Glaciology, 49, 587–598, https://doi.org/10.3189/172756503781830430, 2003.

Price, S. F., Payne, A. J., Howat, I. M., and Smith, B. E.: Committed sea-level rise for the next century from Greenland ice sheet dynamics during the past decade., Proceedings of the National Academy of Sciences of the United States of America, 108, 8978–83, https://doi.org/10.1073/pnas.1017313108, 2011.

Promińska, A., Cisek, M., and Walczowski, W.: Kongsfjorden and Hornsund hydrography – comparative study based on a multiyear survey in fjords of west Spitsbergen, Oceanologia, 59, 397–412, https://doi.org/10.1016/J.OCEANO.2017.07.003, 2017.

Reeh, N., Christensen, E. L., Mayer, C., and Olesen, O. B.: Tidal bending of glaciers: a linear viscoelastic approach, Annals of Glaciology, 37, 83–89, https://doi.org/10.3189/172756403781815663, 2003.

Rignot, E. and Kanagaratnam, P.: Changes in the Velocity Structure of the Greenland Ice Sheet, Science, 311, 986–990, https://doi.org/10.1126/SCIENCE.1121381, 2006.

Rignot, E., Fenty, I., Xu, Y., Cai, C., and Kemp, C.: Undercutting of marine-terminating glaciers in West Greenland, Geophysical Research Letters, 42, 5909–5917, https://doi.org/10.1002/2015GL064236, 2015.

Sato, T. and Greve, R.: Sensitivity experiments for the Antarctic ice sheet with varied sub-ice-shelf melting rates, Annals of Glaciology, 53, 221–228, https://doi.org/10.3189/2012AOG60A042, 2012.

Schellenberger, T., Dunse, T., Kääb, A., Kohler, J., and Reijmer, C. H.: Surface speed and frontal ablation of Kronebreen and Kongsbreen, NW Svalbard, from SAR offset tracking, The Cryosphere, 9, 2339–2355, https://doi.org/10.5194/tc-9-2339-2015, 2015.

Schuler, T. V., Kohler, J., Elagina, N., Hagen, J. O. M., Hodson, A. J., Jania, J. A., Kääb, A. M., Luks, B., Małecki, J., Moholdt, G., Pohjola, V. A., Sobota, I., and Van Pelt, W. J.: Reconciling Svalbard Glacier Mass Balance, Frontiers in Earth Science, 8, 156, https://doi.org/https://doi.org/10.3389/feart.2020.00156, 2020.

Seddik, H., Greve, R., Zwinger, T., Gillet-Chaulet, F., and Gagliardini, O.: Simulations of the Greenland ice sheet 100 years into the future with the full Stokes model Elmer/Ice, Journal of Glaciology, 58, 427–440, https://doi.org/10.3189/2012JOG11J177, 2012.

Shepherd, A., Ivins, E., Rignot, E., Smith, B., Van Den Broeke, M., Velicogna, I., Whitehouse, P., Briggs, K., Joughin, I., Krinner, G., Nowicki, S., Payne, T., Scambos, T., Schlegel, N., Geruo, A., Agosta, C., Ahlstrøm, A., Babonis, G., Barletta, V., Blazquez, A., Bonin, J., Csatho, B., Cullather, R., Felikson, D., Fettweis, X., Forsberg, R., Gallee, H., Gardner, A., Gilbert, L., Groh, A., Gunter, B., Hanna, E., Harig, C., Helm, V., Horvath, A., Horwath, M., Khan, S., Kjeldsen, K. K., Konrad, H., Langen, P., Lecavalier, B., Loomis, B., Luthcke, S., McMillan, M., Melini, D., Mernild, S., Mohajerani, Y., Moore, P., Mouginot, J., Moyano, G., Muir, A., Nagler, T., Nield, G., Nilsson, J., Noel, B., Otosaka, I., Pattle, M. E., Peltier, W. R., Pie, N., Rietbroek, R., Rott, H., Sandberg-Sørensen, L., Sasgen, I., Save, H., Scheuchl, B., Schrama, E., Schröder, L., Seo, K. W., Simonsen, S., Slater, T., Spada, G., Sutterley, T., Talpe, M., Tarasov, L., Van De Berg, W. J., Van Der Wal, W., Van Wessem, M., Vishwakarma, B. D., Wiese, D., and Wouters, B.: Mass balance of the Antarctic Ice Sheet from 1992 to 2017, Nature, 558, 219–222, https://doi.org/10.1038/s41586-018-0179-y, 2018.

Slater, D. A., Nienow, P. W., Goldberg, D. N., Cowton, T. R., and Sole, A. J.: A model for tidewater glacier undercutting by submarine melting, Geophysical Research Letters, 44, 2360–2368, https://doi.org/10.1002/2016GL072374, 2017.

Strozzi, T., Luckman, A., Murray, T., Wegmuller, U., and Werner, C. L.: Glacier Motion Estimation Using SAR Offset-Tracking Procedures, IEEE Transactions on Geoscience and Remote Sensing, 40, 2384–2391, https://doi.org/https://doi.org/10.1109/TGRS.2002.805079, 2002.

Sundfjord, A., Albretsen, J., Kasajima, Y., Skogseth, R., Kohler, J., Nuth, C., Skarðhamar, J., Cottier, F., Nilsen, F., Asplin, L., Gerland, S., and Torsvik, T.: Effects of glacier runoff and wind on surface layer dynamics and Atlantic Water exchange in Kongsfjorden, Svalbard; a model study, Estuarine, Coastal and Shelf Science, 187, 260–272, https://doi.org/10.1016/J.ECSS.2017.01.015, 2017.

Svendsen, H., Beszczynska-Møller, A., Hagen, J. O., Lefauconnier, B., Tverberg, V., Gerland, S., Ørbøk, J. B., Bischof, K., Papucci, C., Zajaczkowski, M., Azzolini, R., Bruland, O., Wiencke, C., Winther, J.-G., and Dallmann, W.: The physical environment of Kongsfjorden-Krossfjorden, an Arctic fjord system in Svalbard, Polar Research, 21, 133–166, https://doi.org/10.1111/j.1751-8369.2002.tb00072.x, 2002.

Todd, J. and Christoffersen, P.: Are seasonal calving dynamics forced by buttressing from ice mélange or undercutting by melting? Outcomes from full-Stokes simulations of Store Glacier, West Greenland, The Cryosphere, 8, 2353–2365, https://doi.org/10.5194/tc-8-2353-2014, 2014.

Todd, J., Christoffersen, P., Zwinger, T., Råback, P., Chauché, N., Benn, D., Luckman, A., Ryan, J., Toberg, N., Slater, D., and Hubbard, A.: A Full-Stokes 3-D Calving Model Applied to a Large Greenlandic Glacier, Journal of Geophysical Research: Earth Surface, 123, 410–432, https://doi.org/10.1002/2017JF004349, 2018.

Todd, J., Christoffersen, P., Zwinger, T., Räback, P., and Benn, D. I.: Sensitivity of a calving glacier to ice-ocean interactions under climate change: New insights from a 3-d full-stokes model, Cryosphere, 13, 1681–1694, https://doi.org/10.5194/TC-13-1681-2019, 2019.

Trusel, L. D., Powell, R. D., Cumpston, R. M., and Brigham-Grette, J.: Modern glacimarine processes and potential future behaviour of Kronebreen and Kongsvegen polythermal tidewater glaciers, Kongsfjorden, Svalbard, Geological Society, London, Special Publications, 344, 89–102, https://doi.org/10.1144/SP344.9, 2010.

Vallot, D., Pettersson, R., Luckman, A., Benn, D. I., Zwinger, T., Van Pelt, W. J. J., Kohler, J., Schäfer, M., Claremar, B., and Hulton, N. R. J.: Basal dynamics of Kronebreen, a fast-flowing tidewater glacier in Svalbard: non-local spatio-temporal response to water input, Journal of Glaciology, 63, 1012–1024, https://doi.org/10.1017/jog.2017.69, 2017.

Vallot, D., Åström, J., Zwinger, T., Pettersson, R., Everett, A., Benn, D. I., Luckman, A., van Pelt, W. J. J., Nick, F., and Kohler, J.: Effects of undercutting and sliding on calving: a global approach applied to Kronebreen, Svalbard, The Cryosphere, 12, 609–625, https://doi.org/10.5194/tc-12-609-2018, 2018.

Van Dongen, E., Jouvet, G., Walter, A., Todd, J., Zwinger, T., Asaji, I., Sugiyama, S., Walter, F., and Funk, M.: Tides modulate crevasse opening prior to a major calving event at Bowdoin Glacier, Northwest Greenland, Journal of Glaciology, 66, 113–123, https://doi.org/10.1017/JOG.2019.89, 2020.

Van Pelt, W. J. J., Oerlemans, J., Reijmer, C. H., Pohjola, V. A., Pettersson, R., and Van Angelen, J. H.: Simulating melt, runoff and refreezing on Nordenskiöldbreen, Svalbard, using a coupled snow and energy balance model, The Cryosphere, 6, 641–659, https://doi.org/10.5194/tc-6-641-2012, 2012.

Weertman, J.: Stability of the Junction of an Ice Sheet and an Ice Shelf, Journal of Glaciology, 13, 3–11, https://doi.org/10.3189/S0022143000023327, 1974.